Cluster spin-glass state with magnetocaloric effect in open framework structure of the Prussian blue analog molecular magnet $K_{2x/3}Cu[Fe(CN)_6]_{2/3}nH_2O$

Pramod Bhatt,[1,2,*] Nilasha Maiti,[1,2] M. D. Mukadam,[1] Sher Singh Meena,[1] A. Kumar,[1,2] and S. M. Yusuf[1,2,†]
[1]*Solid State Physics Division, Bhabha Atomic Research Centre, Mumbai 400 085, India*
[2]*Homi Bhabha National Institute, Anushaktinagar, Mumbai 400 094, India*

(Received 19 January 2023; revised 4 April 2023; accepted 22 June 2023; published 11 July 2023)

We report on the existence of cluster spin-glass behavior and magnetocaloric properties of potassium-ion-intercalated copper hexacyanoferrate open framework material $K_{2x/3}Cu[Fe(CN)_6]_{2/3} \cdot nH_2O$ ($x = 0$ and 0.3) synthesized using a coprecipitate method. The structural properties are investigated using room-temperature powder x-ray and neutron diffraction measurements. The results derived from the fitted x-ray and neutron diffraction data using the Rietveld refinement method reveal that both compounds are in pure single-nanocrystalline phase with face-centered cubic crystal structure of space group Fm-$3m$. The room-temperature Mössbauer spectroscopy reveals the presence of a low-spin (LS) state of Fe^{III} for compound $x = 0$, whereas for compound $x = 0.3$, LS states of Fe^{II} and Fe^{III} are evident. The chemical and Mössbauer studies reveal stoichiometries of compounds as $Cu^{II}[Fe^{III}(CN)_6]_{2/3} \cdot 3.75\,H_2O$ ($x = 0$) compound (1) and $K_{0.2}Cu^{II}[Fe^{II}_{0.3}Fe^{III}_{0.7}(CN)_6]_{2/3} \cdot H_2O$ ($x = 0.3$). The dc magnetization measurement shows a magnetic phase transition from a paramagnetic to a ferromagneticlike state below the magnetic ordering temperatures of ~18.6 and ~16.3 K for the compounds (1) and (2), respectively. The positive value of Curie constants obtained from the fitting of the Curie-Weiss law in the paramagnetic region confirms the presence of ferromagnetic interaction in both compounds. The spin-only effective paramagnetic moments are found to be ~2.3 and ~1.9 μ_B/f.u. for compounds (1), and (2), respectively. The analysis of ac susceptibility measurements as a function of frequency shows that the spin dynamics follows the Vogel-Fulcher and the power law. The best fitted values of $\tau_o = 4.037 \times 10^{-7}$ s and 3.5×10^{-6} s for compounds (1) and (2), respectively, confirm a cluster spin-glass behavior of both compounds. A neutron depolarization study further validates the cluster spin-glass nature of both compounds. The magnetocaloric effect for both the compounds is further investigated and found to be higher for compound (1) than compound (2). The maximum magnetic entropy change—ΔS_M under a magnetic field of 50 kOe is found to be ~6.61 and 2.95 J kg^{-1} K^{-1} for compounds (1) and (2), respectively. The relative cooling power is found to be 78.3 J kg^{-1} for compound (1) and 40 J kg^{-1} for compound (2).

DOI: 10.1103/PhysRevB.108.014412

I. INTRODUCTION

Research and development activities on materials exhibiting the magnetocaloric effect (MCE) have generated great interest recently because of their possible technological application in magnetic refrigeration, i.e., alternative technology for refrigeration [1,2]. Magnetic refrigeration technology is preferable over the conventional gas compression technologies as the former is 20–50% more efficient. The temperature change of magnetic materials during the application of a magnetic field under adiabatic conditions is the measure of MCE. It is generally associated with a large value of magnetization change and depends upon the magnetic entropy change (ΔS_M) or adiabatic temperature change (ΔT_{ad}) and the refrigerant capacity (R_C) of the materials. Such materials with the capability to show magnetic refrigeration (ΔS_M and R_C) are in high demand and offer environmentally friendly efficient energy as alternatives to regular gas-based refrigeration technologies. Therefore, many materials have been studied in recent years for the observation of a significant MCE over a broad temperature range and their suitability in magnetic refrigeration devices. The MCE has mostly been investigated for the intermetallic and alloys [3–5]. However, recently, magnetic materials such as metal-organic frameworks [6–9], high-spin molecular clusters [10–12], organic magnetic molecules [13,14], and Prussian blue analogs (PBAs) [15–17] also have drawn attention as low-temperature magnetic caloric materials. In this regard, the PBA molecular magnets have shown promising results as multifunctional materials [18,19] to exhibit a wide range of magnetic ordering temperatures starting from low to high temperature, hence useful for studying MCE.

The general formula for a PBA-type compound is $AX[Y(CN)_6] \cdot zH_2O$, where A, X, and Y are alkali and transition metal ions. Here, z is the number of water molecules present in the compound. The transition metal ions (X and Y), coordinated to the C ≡ N ligand are in the low-spin (LS) and high-spin states, respectively. The water molecules reside at the interstitial space of the crystal structure. PBAs have mostly cubic structure, and their magnetic and magnetocaloric properties can, therefore, be tailored by varying the

*prabhatt@barc.gov.in
†smyusuf@barc.gov.in

transition metal ions involved in the cyanobridging [20,21]. Moreover, their properties are associated with the synthesis parameters and methods which lead to the porous structure. The $Y(CN)_6$ vacancies also exist in the compounds, but they depend on the stoichiometry of the compound. However, control over the stoichiometries and vacancies is relatively difficult to optimize during the synthesis. Therefore, the MCE in PBAs is not investigated extensively or reported in the literature. The MCE in PBAs has only been reported for a few compounds, particularly the nickel- and chromium-based PBAs. For example, a thin film of the PBA of nickel hexa-cyanochromate deposited by the layer-by-layer method has been studied for the MCE [16]. The maximum entropy changes of 7.43 and 7.07 $J\,kg^{-1}\,K^{-1}$ at 5 T have been reported for parallel and perpendicular configurations, respectively. For $CsNi[Cr(CN)_6]\cdot H_2O$, the highest entropy change is recorded near T_C and found to be $-\Delta S_M = (5.9 \pm 0.7)\,J\,kg^{-1}\,K^{-1}$ [22]. The vacancy-dependent MCE has also been studied in nickel-based PBA $Cs_xNi_4[Cr(CN)_6]_{(8+x)/3}\cdot H_2O$. The vacancies have been controlled during the synthesis, and $-\Delta S_M$ is found to be 6.6 and 6.9 $J\,kg^{-1}\,K^{-1}$ for CsNiCr and $NiCr_{2/3}$, respectively. Similarly, the MCE has been investigated in ternary PBA $Ni_{1.5}[Fe(CN)_6]_x[Cr(CN)_6]_{1-x}\cdot nH_2O$ ($x = 0$, 0.25, 0.5, 0.75, and 1). The maximum value of $-\Delta S$ ($\sim$8.04 $J\,kg^{-1}\,K^{-1}$) has been found for the compound with $x = 1$ under magnetic field of 50 kOe [15]. The value of the MCE for the magnetic materials is maximum at the magnetic ordering temperature. The entropy change is also dependent on magnetic field change as $\Delta S \propto \Delta H^n$, where n is the critical exponent. The present compound, copper hexacyanoferrate in the family of PBAs, is useful for its applications in the fields of batteries, energy storage, ion removal, and biosensors [23–25]. The thermoelectric properties of copper hexacyanoferrate have also been investigated. However, despite many technological applications of copper hexacyanoferrate, its magnetic and magnetocaloric properties have not yet been investigated in detail. Therefore, in this paper, we report on the magnetic and magnetocaloric properties of K^+-ion-intercalated Cu-Fe-based PBA molecular magnets and reveal cluster spin-glass behavior and high entropy change in such open framework materials.

II. EXPERIMENTAL DETAILS

The room-temperature coprecipitation method is used for the synthesis of $K_{2x/3}Cu[Fe(CN)_6]_{2/3}\cdot nH_2O$ ($x = 0$ and 0.3) stoichiometric compounds of PBAs. The chemicals, received from Sigma Aldrich, are of reagent grade and used without further processing. The chemicals $CuCl_2\cdot 2H_2O$ and $K_3[Fe(CN)_6]$ in a 0.15 and 0.1 M molar ratio, respectively, dissolved in aqueous solution and then mixed together to form a compound $Cu[Fe(CN)_6]_{2/3}\cdot nH_2O$ ($x = 0$), whereas for the $x = 0.3$ compound, the Fe^{3+} ions are reduced with 0.1 M $K_2S_2O_3$, resulting in the incorporation of K^+ ions into the structure, which leads to the formation of the mixed-valence $K_{0.2}Cu^{II}[Fe^{II}_{0.5\pm\square}Fe^{III}_{0.5\pm\square}(CN)_6]_{2/3}\cdot mH_2O$ compound. The precipitated compounds are washed many times with distilled water and dried up at room temperature.

A field emission scanning electron microscope (make Carl Zeiss Auriga, with Gemini) with energy-dispersive x-ray analysis is used for surface morphology and chemical analysis. The stoichiometries of the compounds are found to be $Cu[Fe(CN)_6]_{2/3}\cdot 3.75\,H_2O$ and $K_{0.2}Cu^{II}[Fe^{II}_{0.3}Fe^{III}_{0.7}(CN)_6]_{2/3}\cdot H_2O$ for $x = 0$ and 0.3, respectively. The compounds $x = 0$ and 0.3 are denoted further as compounds (1) and (2), respectively. Room-temperature x-ray diffraction (XRD) patterns of both compounds are recorded using a Rigaku diffractometer over an angular (2θ) range of 5°−70° with Cu $K\alpha$ radiation. The analysis of XRD data is carried out using FULLPROF software based on the Rietveld refinement method [26]. The room-temperature neutron diffraction patterns for both compounds are recorded (wavelength $\lambda = 1.094$ Å) using a neutron powder diffractometer, at Dhruva reactor, Trombay, India. The neutron depolarization experiments are carried out using the polarized neutron spectrometer [27] at Dhruva reactor, Trombay, India.

Room-temperature Mössbauer spectroscopy in transmission geometry with the constant acceleration mode is used for determination of the ionic state and local surroundings of Fe ions in both compounds. The Co–57 source in Rh matrix of strength 50 mCi is used for this purpose. Further, the magnetic properties are investigated in detail using temperature-dependent dc magnetization measurements in field-cooled (FC) conditions down to 5 K using a Cryogenic Ltd., UK, make commercial magnetic properties measurement system. The magnetization data vs field at 5 K are measured over an applied magnetic field of ±50 kOe for both compounds. The ac susceptibility study as a function of frequency in the low-temperature region is also carried out to investigate the spin dynamics of both magnetic compounds. For the magnetocaloric study, the FC magnetization measurements over the magnetic ordering temperature are measured at various external magnetic fields for both compounds.

III. RESULT AND DISCUSSION

A. X-ray and neutron diffraction study

The Rietveld refined room-temperature x-ray and neutron powder diffraction patterns of both compounds are shown in Fig. 1. The refinement shows that both compounds are in a pure single-crystalline phase with a cubic structure of the space group Fm-3m. The important structural parameters, derived from the combined Rietveld analysis of x-ray and neutron diffraction data, are shown in Table I.

The lattice parameters are found to be $\sim$10.128 ± 0.001 and 9.997 ± 0.004 Å for compounds (1) and (2), respectively. The observed slight decrease in lattice constant for compound (2) as compared with compound (1) could be due to smaller bond lengths of Cu-N and Fe-C and the presence of more electrons, which are introduced by the reduction of $[Fe^{III}(CN)_6]$ to $[Fe^{II}(CN)_6]$. The schematic crystal structures of both compounds, as obtained from the Rietveld refinement, are shown in Fig. 2. It is observed that both compounds are crystallized into a cubic crystal structure in which transition metal ions Cu^{II} and Fe^{III} occupy the 4a (0, 0, 0) and 4b ($\frac{1}{2}$, $\frac{1}{2}$, $\frac{1}{2}$) crystallographic sites, respectively. The alkali metal ions K^+ occupy

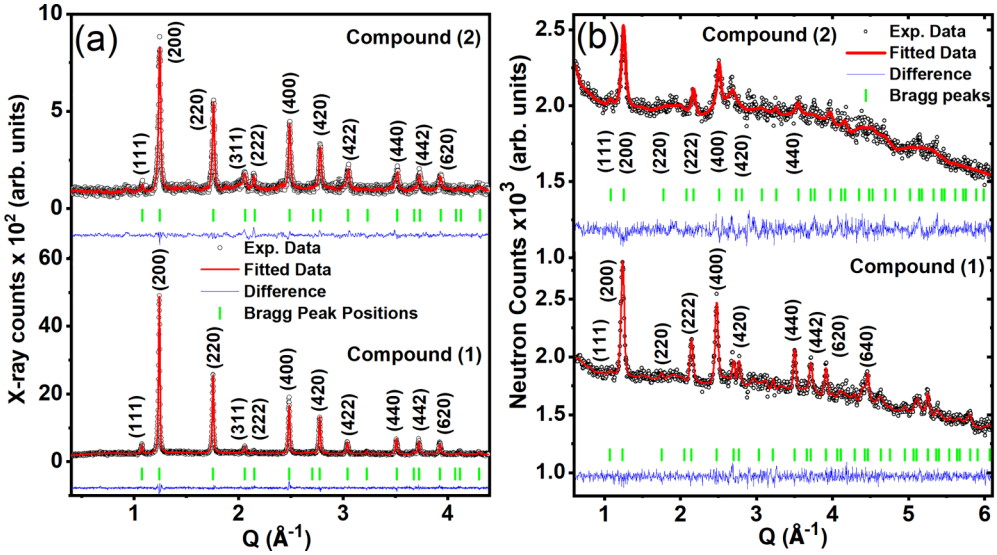

FIG. 1. The Rietveld refined room-temperature (a) x-ray diffraction and (b) neutron diffraction patterns of compounds (1) and (2). The experimentally observed and fitted patterns are shown by the open circles and solid lines, respectively. The difference between experimental and fitted patterns is shown by the solid lines at the bottom. The positions of allowed Bragg peaks are shown by vertical lines. The (*hkl*) values of the Bragg peaks are also marked for both compounds.

some of the interstitial sites of uncoordinated water molecules in compound (2), as shown in Fig. 2.

It has been observed that totals of ∼3.75 and ∼1 water molecules are present in compounds (1) and (2), respectively. The water molecules, which occupy the interstitial sites of 8*c* and 32*f* in the crystal structure, are known as uncoordinated water, whereas the water molecules which are connected to N atoms (situated at 24*e* sites) are known as coordinated water. The crystallite size in the compound is derived using

$$\tau = \frac{K\lambda}{t\cos\theta},$$

where τ is the mean size of the crystalline domains, K is a dimensionless shape factor with a value close to unity (0.9), λ is the x-ray wavelength, and t is the line broadening at half the maximum intensity. Using the most intense Bragg peak, the average crystallite sizes are estimated to be ∼350 ± 15 and ∼220 ± 10 Å for compounds (1) and (2), respectively. The refinement results, obtained from the fitting of neutron diffraction data, are consistent with the XRD results. The background in the neutron diffraction patterns of both compounds is due to the hydrogen of the compounds. The PBAs exhibit structural disorder which arises due to vacancies and clustering of uncoordinated water molecules in the compounds evident from the neutron diffraction results [28].

B. Mössbauer spectroscopy study

Mössbauer spectroscopy is carried out to find out the spin states and local atomic environment of Fe atoms in both compounds. Figure 3 shows fitted Mössbauer spectra at room temperature, recorded at a velocity of 4.0 mm/s, of both

TABLE I. Rietveld refined structural parameters for compounds (1) and (2). The fractional coordinates are denoted as x', y', and z'.

	Atom	Wyckoff site	x'	y'	z'	Occupancy
Compound (1)	Cu	4*a*	0	0	0	1
Fm-3*m*	Fe	4*b*	0.5	0.5	0.5	0.67
$a = 10.128 \pm 0.001$	C	24*e*	0.322(3)	0	0	0.67
$b = 10.128 \pm 0.001$	N	24*e*	0.197(7)	0	0	0.67
$c = 10.128 \pm 0.001$	O_1	24*e*	0.237(2)	0	0	3.09(2)
	O_2	32*f*	0.309(5)	0.309(5)	0.309(5)	0.51(4)
	O_3	8*c*	0.25	0.25	0.25	0.42(4)
Compound (2)						
Fm-3*m*	Cu	4*a*	0	0	0	1
$a = 9.997 \pm 0.004$	Fe	4*b*	0.5	0.5	0.5	0.67
$b = 9.997 \pm 0.004$	C	24*e*	0.306(3)	0	0	0.67
$c = 9.997 \pm 0.004$	N	24*e*	0.189(5)	0	0	0.67
	O_1	24*e*	0.207(2)	0	0	1.11(5)
	O_2	32*f*	0.333(7)	0.333(7)	0.333(7)	0.06(4)
	K	8*c*	0.25	0.25	0.25	0.19(7)

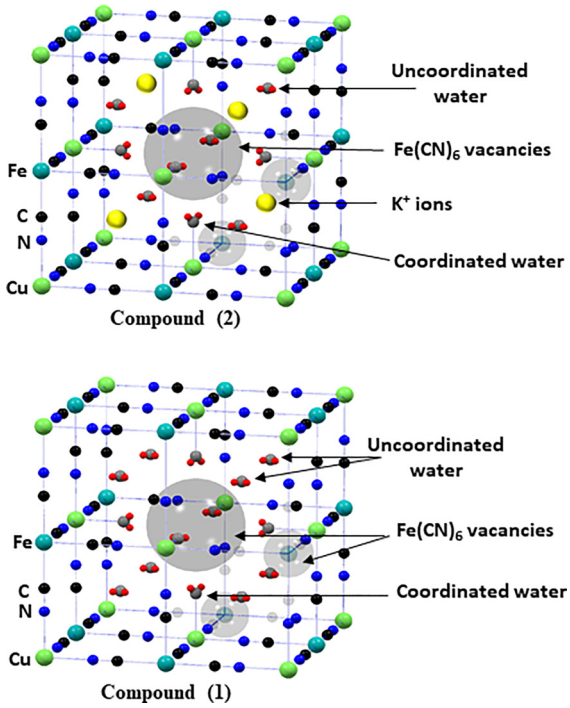

FIG. 2. Schematic crystal structure of compounds (1) and (2). The positions of $Fe(CN)_6$ vacancies and coordinated and uncoordinated water molecules are shown in the cubic crystal structure. The crystallographic positions of some of the K^+ ions in compound (2) are marked at interstitial sites.

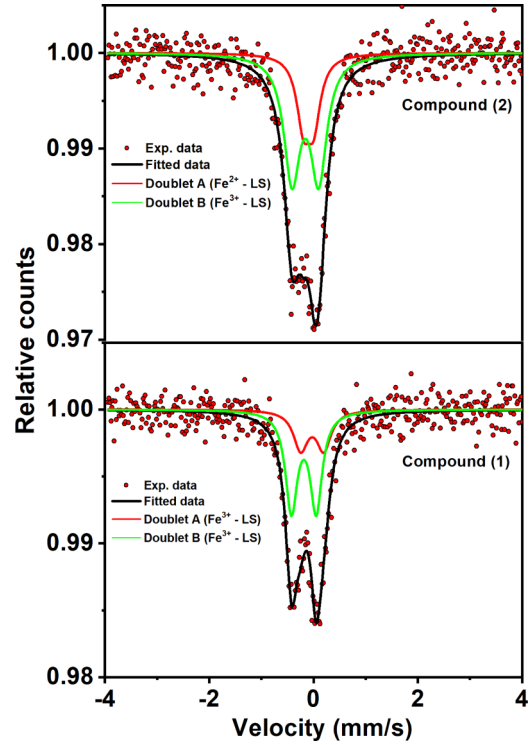

FIG. 3. Room-temperature Mössbauer spectra of compounds (1) and (2). The recorded experimental and least-squares fitted data are shown by the open circles and thick solid lines, respectively.

compounds. The absence of the magnetic six-line hyperfine pattern confirms that both compounds are in paramagnetic ground state at room temperature. The fitted Mössbauer parameters, such as isomer shift (δ), quadrupole splitting (ΔE_Q), and line width (Γ), for both compounds are listed in Table II. The fitting of the data for compound (1) indicates the presence of two paramagnetic doublets (A and B) with isomer shifts (δ) of ~ -0.026 and -0.188 for doublets A and B, respectively. The values of isomer shift (δ) and quadrupole splitting (ΔE_Q) suggest that Fe ions are in +3 LS state in compound (1). Further, these two doublets suggest two different environments of Fe in compound (1). The different δ values of these doublets are due to two different environments of Fe, which is evident from the schematic diagram (Fig. 2) of the crystal structure. The Fe has two different environments: (i) the Fe atoms connected to Cu, which is ∼64%, and (ii) the Fe atoms connected to N atoms attached with coordinated molecules water, which is ∼36%. The Mössbauer spectra of compound (2) are fitted with two symmetric doublets. The δ values of both doublets are found to be -0.098 mm/s (doublet A) and 0.156 mm/s (doublet B), respectively. The observed δ values indicate that doublet A is due to LS Fe^{+2} ions, whereas doublet B belongs to LS Fe^{+3} ions. The areas under these two doublets A and B (Table II) are found to be ∼29.9% (LS Fe^{+2}) and ∼70.1% (LS Fe^{+3}), respectively. The reduction of Fe^{+3} may lead to the formation of some of the Fe^{+2} spin state in compound (2). The higher value of ΔE_Q for doublet B than doublet A in compound (1) indicates the presence of a relatively larger crystal field gradient at the Fe site, connected with Cu atoms. The higher value of ΔE_Q for doublet B confirms more distortion at these Fe sites, whereas for compound (2), the ΔE_Q value for

TABLE II. Hyperfine parameters for compound (1) and compound (2).

Sample	Fe-site and ionic state	Isomer shift (δ), (mm/s)	Quadrupole splitting (ΔE_Q), (mm/s)	Line width (Γ), (mm/s)	Relative area (%)	Goodness of fit (χ^2)
Compound (1)	Doublet A (Fe^{3+} LS)	-0.026 ± 0.008	0.443 ± 0.005	0.332 ± 0.005	35.9 ± 0.5	0.87
	Doublet B (Fe^{3+} LS)	-0.188 ± 0.002	0.475 ± 0.004	0.278 ± 0.003	64.1 ± 0.5	
Compound (2)	Doublet A (Fe^{2+} LS)	-0.098 ± 0.005	0.200 ± 0.005	0.322 ± 0.04	29.9 ± 0.5	0.92
	Doublet B (Fe^{3+} LS)	-0.156 ± 0.005	0.518 ± 0.006	0.371 ± 0.004	70.1 ± 0.5	

doublet B is higher (∼0.518 mm/s) than doublet A, suggesting that the distortion increases at LS Fe^{+3} sites due to inclusion of K in the structure. The Mössbauer results confirm that Fe is in Fe^{+3} LS state with two different environments arising due to Fe connected to C ≡ N without and with water molecules, whereas in compound (2), both LS states of Fe^{+2} and Fe^{+3} exist with relative areas of 30 and 70%, respectively, due to inclusion of K ions in the crystal structure. The identification of spin states and their doublet for Fe ions is analyzed based on the δ values. The δ value for LS Fe^{+2} is in the range of −0.2 to 0.5, whereas it is −0.5 to 0.4 for LS Fe^{+3} [29,30]. Based on Mössbauer spectroscopy, the stoichiometries of the compounds are found to be $Cu[Fe(CN)_6]_{2/3} \cdot 3.75\,H_2O$ and $K_{0.2}Cu^{II}[Fe^{II}_{0.3}Fe^{III}_{0.7}(CN)_6]_{2/3} \cdot H_2O$ for $x = 0$ [compound (1)] and 0.3 [compound (2)], respectively.

Both compounds have a three-dimensional (3D) network of Cu−N ≡ C−Fe−C ≡ N−Cu, in which Cu and Fe atoms are octahedrally surrounded by −N ≡ C− and −C ≡ N− units, which could show Jahn-Teller distortion due to the presence of $Cu^{+2}(d^9)$ ions and consequently affect the magnetic properties of these compounds. The distortion and its influence on the structural properties of PBAs have been reported in the literature. For example, a cubic-to-tetragonal structural phase transition in rubidium manganese hexacyanoferrate [31] and a reduction of crystal symmetry to tetragonal caused by the strong cooperative Jahn-Teller effect of Cu^{2+} ions in $CsCu[Cr(CN)_6] \cdot 2.1\,H_2O$ have been reported [32]. For the present compounds, with nearly an ideal octahedral geometry, lowering of the crystal symmetry has not been observed as a function of temperature. However, a 3D network of octahedral coordination units of $CuN_4(H_2O)_2$ is expected to induce Jahn-Teller distortion in these compounds. The Jahn-Teller distortion can lead to the change in the strength of magnetic exchange coupling constants. In fact, the quadrupole splitting (Table II), obtained from the Mössbauer study at room temperature, is clear evidence of the presence of Jahn-Teller distortion in these compounds. The Jahn-Teller distortion is expected to be slightly higher in compound (1) than compound (2) due to presence of more $CuN_4(H_2O)_2$ octahedral units in compound (1).

C. DC magnetization study

Figure 4 shows the FC magnetization (M) vs temperature (T) curves under an external applied magnetic field of 200 Oe for both compounds. The compounds show a paramagnetic-to-ferromagneticlike transition with decreasing temperature. Magnetic transitions at ∼18.6 and ∼16.3 K have been observed from the magnetization data and could be ferromagnetic or ferrimagnetic in nature. The magnetic ordering temperature has been estimated from the first derivative of M vs T data.

The magnetic susceptibility (χ) is measured as a function of temperature. Figure 5 shows χT vs T curves at 200 Oe for both compounds. The χT vs T curves rise continuously with the lowering of temperature until the transition temperature is reached for both compounds, which is a characteristic behavior of ferromagnetic materials.

The inverse of the susceptibility (χ^{-1}) as a function of temperature is shown in the inset of Fig. 5. The paramagnetic

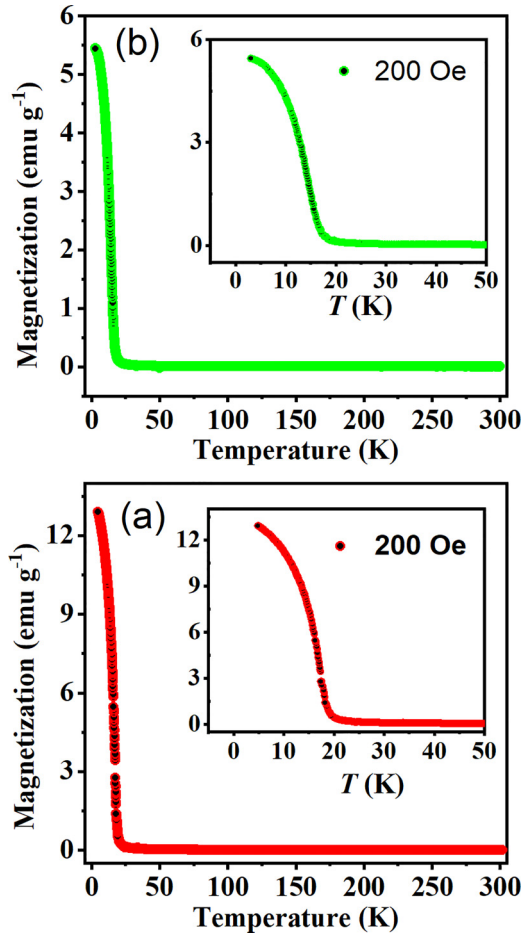

FIG. 4. (a) and (b) show the field-cooled magnetization vs temperature curves for compounds (1) and (2), respectively, under an external applied magnetic field of 200 Oe. The inset shows the magnetic ordering transition in the magnetified range of temperature 5–50 K.

region of the susceptibility is fitted using the Curie-Weiss law:

$$\chi = \frac{C}{T - \theta_p},$$

where θ_p is the paramagnetic Curie temperature, and C is the Curie constant. The positive values of θ_p (18 and 16 K) for compounds (1) and (2), respectively, confirm the presence of the ferromagnetic interaction in both compounds. The spin-only effective paramagnetic moments μ_{eff} are also calculated using $(3Ck_B/N_A)^{1/2}\,\mu_B \sim (8C)^{1/2}\,\mu_B$, where N_A is Avogadro's number and k_B is the Boltzmann constant, which is found to be ∼2.3 and ∼1.9 μ_B/f.u. The theoretically expected (spin-only) values of μ_{eff} are calculated by using the formula $(\mu_{eff})^2 = \Sigma[g^2\{nS(S+1)\}]\mu_B^2$, where g is gyromagnetic ratio (∼2), n is the number of magnetic ions with spin S in formula units, and summation Σ runs over all magnetic ions in formula units. The theoretically calculated values of spin-only μ_{eff} are found to be 2.45 μ_B/f.u. for compound (1), assuming Fe^{+3} in their LS states ($S = \frac{1}{2}$), whereas Cu is in high-spin state ($S = \frac{1}{2}$). However, for compound (2), ∼70% Fe^{+3} ions are in LS state ($S = \frac{1}{2}$), while ∼30% are in Fe^{+2} LS state ($S = 0$), as obtained from the Mössbauer study. The

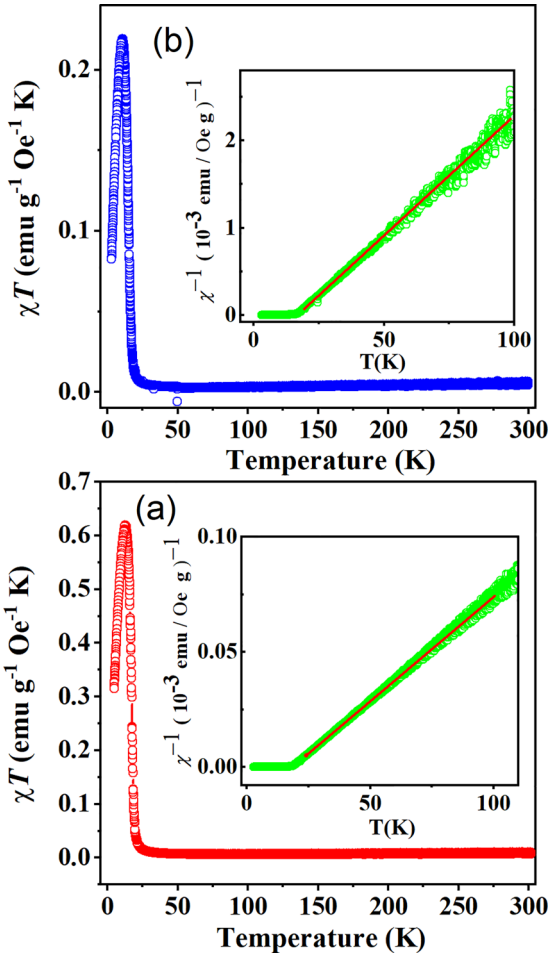

FIG. 5. (a) and (b) show χT vs temperature (T) curves for compounds (1) and (2), respectively. The inverse susceptibility vs temperature curves, fitted by using the Curie-Weiss law, are shown in the inset.

theoretically calculated spin-only value of μ_{eff} for compound (2) is found to be 2.24 μ_B/f.u. The experimentally observed values of μ_{eff} are consistent with the theoretically calculated spin-only values of both compounds.

Figure 6 shows the magnetization (M) as a function of the applied magnetic field (H) for both compounds at ±5 Tesla. The coercivity values of ∼2 and 3 kOe have been found for compounds (1) and (2), respectively, whereas the maximum saturation magnetization values of ∼1.5 and 0.92 μ_B/f.u. have been observed for compounds (1) and (2), respectively. The shape of the M-H loops indicates a ferromagnetic nature of the compound. The theoretically expected (spin-only) value of the ordered magnetic moment μ_s per formula unit is calculated by using the formula $\mu_s = \Sigma(gnS)\mu_B$, where g is the gyromagnetic ratio (∼2), n is the number of magnetic ions, and S is the spin of the magnetic ions. The μ_s per formula unit (spin-only) values are found to be 1.67 and 1.46 μ_B/f.u. for compounds (1) and (2), respectively. The Mössbauer study reveals that ∼30% of Fe is in LS Fe^{+2} state, whereas ∼70% is in the Fe^{+3} LS state. The difference in the experimentally observed and theoretically calculated ordered moments is due to the nonsaturation of the hysteresis curves. The magnetization study confirms a ferromagnetic nature of both compounds.

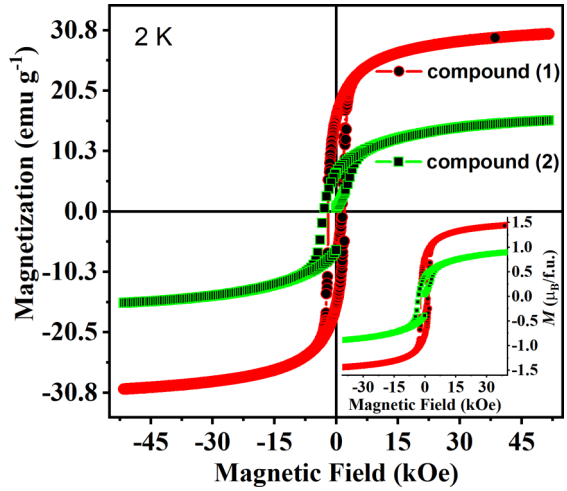

FIG. 6. Magnetization (M) vs field (H) curves at 2 K for both compounds up to 50 kOe. The inset shows the corresponding M vs H curve in Bohr magnetron (μ_B) per f.u.

D. AC susceptibility study

Figure 7 shows ac magnetic susceptibility data for both compounds. The ac magnetic field amplitude of 2 Oe is applied in the temperature range of 5–25 K. Both the in-phase (χ') and out-of-phase (χ'') susceptibilities exhibit peaks at around $T_P \sim 16.8$ K. The in-phase susceptibility (χ') changes with respect to frequency. The peak maxima of the in-phase (χ') susceptibility are frequency dependent for both

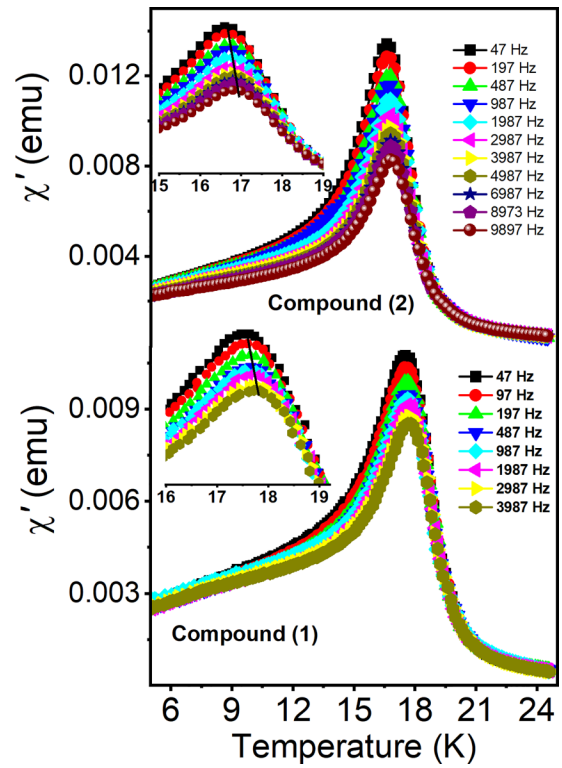

FIG. 7. The frequency dependence in-phase (χ') magnetic ac susceptibility for both compounds as a function of temperature. The inset shows the magnified region of the ac susceptibility data.

compounds. The characteristic peak temperatures (T_P) are found to be ∼17.3 and ∼16.4 K at low frequency of 47 Hz for compounds (1) and (2), respectively. The peak amplitude decreases, and peak maxima systematically shift to higher temperatures and are found to be at ∼17.8 and ∼16.8 K for higher frequency of 3987 Hz for compounds (1) and (2), respectively. This is expected for a compound with ferromagnetic or ferrimagnetic ordering having long-range magnetic correlations. The frequency-dependent ac susceptibility reveals the spin behavior and nature of the magnetic ordering in the compounds. It is known that the anomaly in ac susceptibility depends on the excitation frequency. When the position of peak maxima shifts to a higher temperature with the increasing frequency, it indicates the characteristic feature of superparamagnets and spin-glass-type ordering [33,34].

The ac susceptibility data are further analyzed in terms of relaxation time τ, experimentally measured characteristic time which describes the dynamical fluctuation over observation time t. Since the characteristic relaxation time at the in-phase susceptibility maximum of the system corresponds to the observation time, we can write $t = 1/f$. The relaxation of spin-glass and superparamagnetic clusters follows the Néel-Arrhenius law. The relaxation time τ is calculated from the maximum of the susceptibility curve using the Arrhenius law:

$$\tau = \tau_0 \exp\left(\frac{E_a}{k_B T}\right), \tag{1}$$

where τ is the relaxation time, τ_0 is the pre-exponential factor, and E_a is the energy barrier. Figure 8 shows $\ln(f)$ vs $1/T_P$ fitting of experimental data using the Néel-Arrhenius law. The fitted values of τ_0 and E_a/k_B are found to be $\sim 2.1 \times 10^{-171}$ s and 6841 K for compound (1), which are totally unphysical and unrealistic. However, the frequency dependence of freezing temperature is fitted well to the empirical Vogel-Fulcher law, which considers intercluster interaction:

$$\tau = \tau_0 \exp\left[\frac{E_a}{k_B(T_P - T_0)}\right], \tag{2}$$

where T_P is the peak temperature in Fig. 7, and the values of T_0 and E_a are obtained from the fitting. Here, k_B is the Boltzmann constant. The interactions between the superparamagnetic clusters are governed by the term $(T_P - T_0)$. The fitting of Eq. (2) gives the characteristic frequency $(1/\tau_0)$, the activation energy barrier (E_a), and the temperature $T_0 = 17.38(1)$ for compound (1). Thus, E_a/k_B and T_0 can be obtained from the slope and intercept of the $\ln(f)$ vs T_P plot, as shown in Fig. 8. Figure 8 shows the fitted curve using the Vogel-Fulcher law, and the fitted parameters are found to be $E_a/k_B = 1.5$ K and $\tau_0 = 4.037 \times 10^{-7}$ s for compound (1). Similarly, the best fit values are found to be $E_a/k_B = 0.2$ K and $T_0 = 16.6(3)$ K for compound (2). The value of relaxation time τ_0 is found to be 3.5×10^{-6} s for compound (2). The larger value of τ_0 is expected for interacting magnetic spin clusters (τ_0 lies in the range $\sim 10^{-6}$ to 10^{-10} s), which is mainly due to slow dynamics, and matches well with the previously reported values of several other cluster spin-glass-type compounds [35–37]. For canonical spin-glass compounds, the value of τ_0 ($\sim 10^{-13}$ to 10^{-14}) is several orders of magnitude smaller than that of the cluster spin glasses. Thus, based on the ac susceptibility fitted parameters, it can be revealed that both compounds exhibit cluster spin-glass behaviors [38].

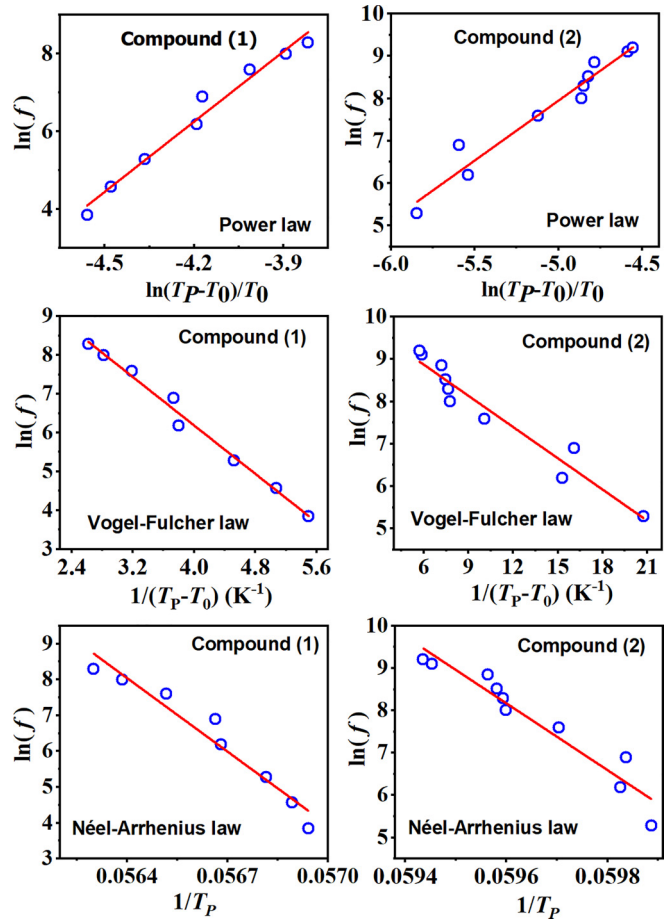

FIG. 8. The bottom figures show the $\ln(f)$ vs $1/T_P$ plot for both compounds. The data are fitted by a solid line using least-squares fitting by considering the Néel-Arrhenius equation. The figures in the middle show $\ln(f)$ vs $1/(T_P - T_0)$ plot for both compounds, fitted using the Vogal-Fulcher law. The top panel shows a log-log plot of the frequency vs $(T_P - T_0)/T_0$, fitted by using the power law.

Though both the Néel-Arrhenius and Vogel-Fulcher laws are used to confirm the nature of magnetic ordering in spin-glass, cluster spin-glass, and superparamagnetic systems, there is a further important criterion (as used below), based on a power law, to check the magnetic ordering nature of the compound. We have analyzed our frequency-dependent ac susceptibility data using the power law described below:

$$\tau(T_P) = \tau_0\left(\frac{T_P}{T_g} - 1\right)^{-z\nu}, \tag{3}$$

where T_g is freezing temperature, τ_0 is related to the relaxation of the individual cluster magnetic moment, and $z\nu$ is a critical exponent. The best fitted values of $\tau_0 = 2.04 \times 10^{-12}$ s and 2.54×10^{-9} s are found for compounds (1), and (2), respectively. The values of critical exponent $z\nu$ are found to be 6.01 and 4.82 for compounds (1) and (2), respectively. The critical exponent value lies between 4 and 12 for spin-glass compounds. The values derived from the power law are different from the values obtained using the Vogel-Fulcher law;

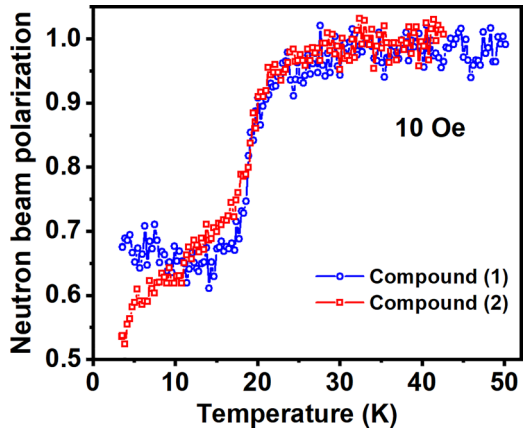

FIG. 9. Neutron depolarization curves at 10 Oe for compounds (1) and (2).

however, they are acceptable for a cluster spin-glass compound. The larger values of τ_0 only reflect nanosized spin clusters instead of single atomic spins in these compounds. The analysis of ac susceptibility data confirms that both compounds exhibit cluster spin-glass-like behavior with freezing temperatures of 17.3 and 16.5 K. The observation of spin-glass-type behavior is also reported in other PBA compounds [33,39–43].

E. Neutron depolarization study

Figure 9 shows the neutron depolarization data for compounds (1) and (2). In a neutron depolarization study, polarized neutrons, while passing through ferromagnetic/ferrimagnetic samples, get depolarized owing to the Larmor precession of neutron spins in the magnetic fields of randomly oriented magnetic domains inside the sample and provide information about size/magnetization of domains [21,44–46]. Both compounds show finite depolarization of the polarized neutron beam $<\sim$20 K, indicating the onset of ferromagnetic/ferrimagnetic-type correlations. Compound (2) has a slightly lower T_C than that of compound (1) and is consistent with our dc magnetization study. At the lowest temperature of 3 K, compound (2) shows slightly larger depolarization, and this may be related to the slower relaxation rate of magnetic spin clusters in compound (2) than compound (1). The neutron beam polarization curve for compound (2) shows a continuous decrease in polarization value with decreasing temperature. This is in contrast with nearly constant depolarization just below T_C for compound (1) probably due to relatively slower spin dynamics in compound (2) than compound (1). The neutron depolarization data are consistent with the ac susceptibility study, confirming cluster spin-glass behavior.

F. Magnetocaloric study

The magnetocaloric study is carried out in terms of the entropy change $(-\Delta S_M)$ for both compounds as a function of applied magnetic field (H). It can be expressed using the

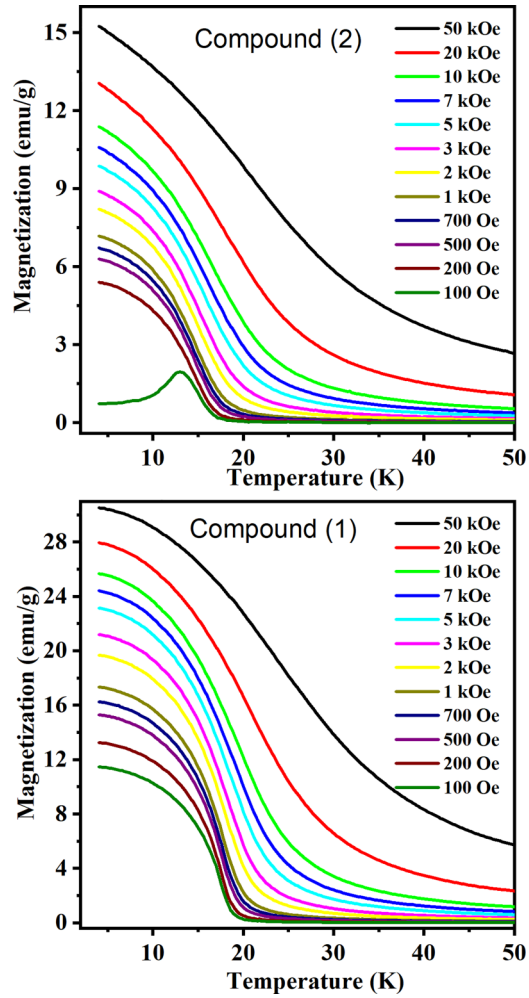

FIG. 10. The temperature-dependent magnetization at different applied magnetic fields for both compounds.

Maxwell relation, i.e., the change in M with respect to T:

$$\left(\frac{\partial S}{\partial H}\right)_T = \left(\frac{\partial M}{\partial T}\right)_H. \tag{4}$$

The magnetic entropy change (ΔS_M) is calculated using

$$(\Delta S_M)_{H,\,T} = \int_0^H \left[\frac{\partial M_{(H,\,T)}}{\partial T}\right]_H dH. \tag{5}$$

The dc magnetization data as a function of temperature for both compounds at various applied magnetic fields up to 50 kOe are shown in Fig. 10. The measurements are carried out in zero-FC condition to avoid the memory effect due to cooling under field. The magnetization curve rises slowly with applied fields. With decreasing temperature, an enhancement of magnetization and a paramagnetic-to-ferromagneticlike transition is observed for both compounds. Moreover, the magnetic ordering temperature is found to shift to higher temperature with increasing applied magnetic field.

The value of $-\Delta S_M$ is calculated using Eq. (5) as a function of temperature with respect to various applied magnetic fields for each temperature. The maximum magnetic entropy change is expected near the magnetic transition or ordering

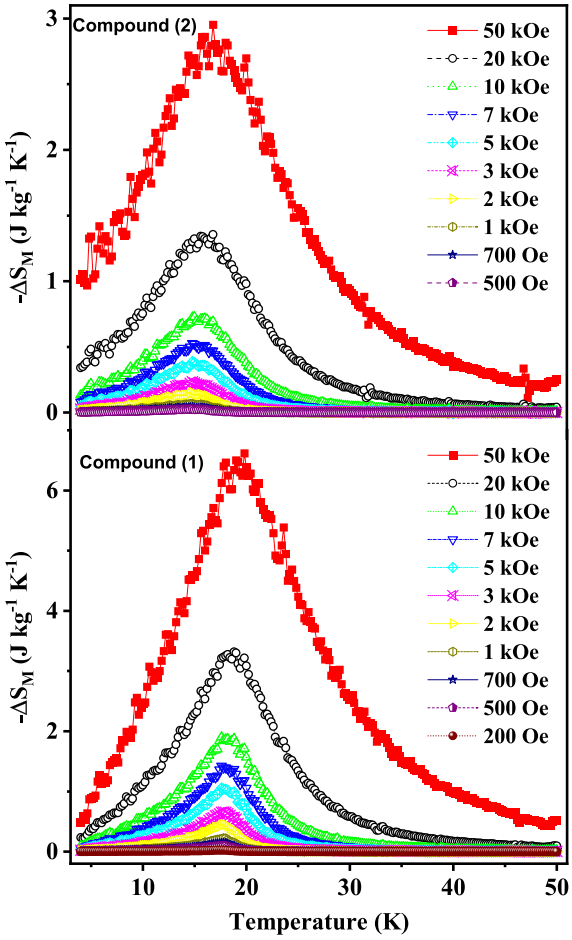

FIG. 11. Magnetic entropy change $-\Delta S_M$ as a function of temperature for the various values of ΔH for compounds (1) and (2).

temperature. Figure 11 shows the $-\Delta S_M$ vs T curves for the various values of ΔH for both compounds. It is observed that the value of $-\Delta S_M$ increases with an increasing applied magnetic field with a peak near the paramagnetic-to-ferromagnetic phase transition temperature. The maximum value of $-\Delta S_M$ is found to be ~6.61 and ~2.95 J kg^{-1} K^{-1} for compounds (1) and (2), respectively. The values of $-\Delta S_M$ found for both

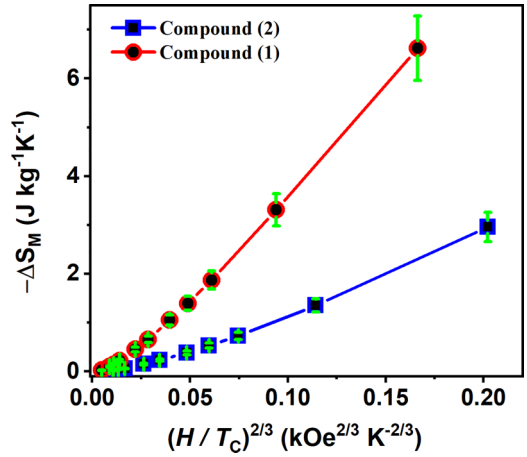

FIG. 12. The magnetic entropy change $-\Delta S_M$ as a function of $(H/T_C)^{2/3}$ for both compounds.

compounds are comparable with the values for other similar PBAs presented in Table III.

Here, $-\Delta S_M$ is also presented as a function of $(H/T_C)^{2/3}$ for both compounds, as shown in Fig. 12. A linear relationship between $-\Delta S_M$ and $(H/T_C)^{2/3}$ is evident for both compounds. However, the lattice entropy contribution is not considered in linear relations, indicating the lattice contribution is either negligible or constant. The linear relation between $-\Delta S_M$ and $(H/T_C)^{2/3}$ shows the critical behavior of the spin system and information related to second-order phase transition. According to mean-field theory, it is already established that, near the vicinity of a second-order phase transition, the value of (H/T_C) is $\sim\frac{2}{3}$ [48].

The relative cooling power (RCP) or refrigerant capacity has also been estimated for both compounds. It is the parameter which provides an estimate of the heat transfer during one ideal refrigeration cycle between the cold and hot heat sinks. The shaded region in Fig. 13(a) represents the RCP for both compounds. The RCP is estimated by integrating the area under the $-\Delta S_M$ vs T curves as

$$\mathrm{RCP} = \int_{T^{\mathrm{cold}}}^{T^{\mathrm{hot}}} \Delta S_M(T)dT.$$

TABLE III. Comparison between the maximum magnetic entropy change $-\Delta S_M$ and the RCP for the present compounds and other similar PBAs reported in the literature.

Compounds	T_C (K)	H (kOe)	$-\Delta S_M$ (J kg^{-1} K^{-1})	RCP (J kg^{-1})	References
$Cu[Fe(CN)_6]_{2/3} \cdot 3.75\,H_2O$	18.6	50	6.61	78.3	This paper
$K_{0.2}Cu^{II}[Fe^{II}_{0.3}Fe^{III}_{0.7}(CN)_6]_{2/3} \cdot 1H_2O$	16.3	50	2.95	40.0	This paper
$Ni_3[Cr(CN)_6]_2 \cdot 15H_2O$	60	50	6.49	273.07	[15]
$Ni_3[(Cr(CN)_6)_{1.5}Fe(CN)_6)_{0.5}] \cdot 15\,H_2O$	52	50	5.78	273.33	[15]
$Ni_3[(Cr(CN)_6)_1Fe(CN)_6)_1] \cdot 15\,H_2O$	41	50	5.47	235.84	[15]
$Ni_3[(Cr(CN)_6)_{0.5}Fe(CN)_6)_{1.5}] \cdot 15\,H_2O$	33	50	6.06	208.62	[15]
$Ni_3[(Fe(CN)_6)]_2 \cdot 15H_2O$	22	50	8.04	145.35	[15]
$Cs_xNi_4[(Cr(CN)_6)]_{(8+x)/3} (x = 0)$	60	70	6.9		[47]
$Cs_xNi_4[(Cr(CN)_6)]_{(8+x)/3} (x = 4)$	90	70	6.6		[47]
$CsNi[(Cr(CN)_6)] \cdot H_2O$	90	70	6.6		[22]
$Cr_3[(Cr(CN)_6)]_2 \cdot 12\,H_2O$	230	70	0.93		[22]

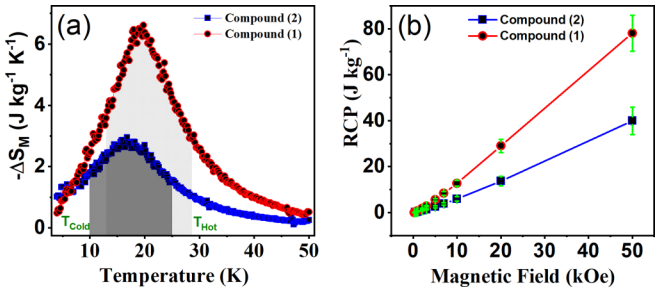

FIG. 13. (a) The shaded area shows the relative cooling power (RCP) for both compounds. (b) The RCP as a function of applied magnetic field.

Here, T^{cold} and T^{hot} are the lower and higher temperatures at half maximum of the $-\Delta S_M$ peak in the $-\Delta S_M$ vs T curve and can be considered the temperatures of the cold and hot reservoirs, respectively. The highest values of RCP are found to be ∼78.3 and 40 J kg^{-1} for compounds (1) and (2), respectively, for $\Delta H = 5$T, which is comparable with the values that are reported in the literature for other PBAs listed in Table III. The RCP increases linearly with increasing magnetic field, as shown in Fig. 13(b).

IV. CONCLUSIONS

Potassium-ion-intercalated copper hexacyanoferrate open framework materials, $K_{2x/3}Cu[Fe(CN)_6]_{2/3} \cdot nH_2O$ [$x = 0$ for compound (1) and $x = 0.3$ for compound (2)] are synthesized using a coprecipitate method. The combined x-ray and neutron diffraction study reveals that both compounds are in a pure single-crystalline cubic phase (space group Fm-$3m$). The Mössbauer spectroscopy study reveals LS states of Fe^{III} and Fe^{II} for compound (2). The ferromagnetic ordering temperatures are found to be ∼18.6 and ∼16.3 K for compounds (1) and (2), respectively. The cluster spin-glass behavior has been established for both compounds which are analyzed using the frequency-dependent ac susceptibility following the Vogel-Fulcher and power laws. The relaxation times are found to be $\sim 4.03 \times 10^{-7}$ s and 3.5×10^{-6} s for compounds (1) and (2), respectively. The neutron depolarization study supports the ac susceptibility analysis of having cluster spin-glass behavior of both compounds. Moreover, these compounds exhibit enhanced magnetocaloric properties near the transition temperature with maximum magnetic entropy change ($-\Delta S_M$) values of ∼6.61 and 2.95 J kg^{-1} K^{-1} under a magnetic field of 50 kOe for compounds (1) and (2), respectively. The corresponding RCP is found to be 78.3 J kg^{-1} for compound (1) and 40 J kg^{-1} for compound (2). In this paper, we demonstrate that the open framework structure of copper-hexacyanoferrate-based PBAs exhibits multifunctional behavior.

ACKNOWLEDGMENTS

P.B. would like to thank A. Jain and V. B. Jayakrishnan for their help in the neutron and XRD measurements, respectively.

[1] J. K. A. Gschneidner and V. K. Pecharsky, Magnetic refrigeration materials (invited), J. Appl. Phys. **85**, 5365 (1999).
[2] J. R. Gomez, R. F. Garcia, A. D. M. Catoira, and M. R. Gomez, Magnetocaloric effect: A review of the thermodynamic cycles in magnetic refrigeration, Renewable Sustainable Energy Rev. **17**, 74 (2013).
[3] S. B. Roy, Chapter two—Magnetocaloric effect in intermetallic compounds and alloys, Handb. Magn. Mater. **22**, 203 (2014).
[4] M. Ovichi, H. Elbidweihy, E. D. Torre, L. H. Bennett, M. Ghahremani, F. Johnson, and M. Zou, Magnetocaloric effect in NiMnInSi Heusler alloys, J. Appl. Phys. **117**, 17D107 (2015).
[5] T. Krenke, E. Duman, M. Acet, E. F. Wassermann, X. Moya, L. Mañosa, and A. Planes, Inverse magnetocaloric effect in ferromagnetic Ni–Mn–Sn alloys, Nat. Mater. **4**, 450 (2005).
[6] V. Zeleňák, M. Almáši, A. Zeleňáková, P. Hrubovčák, R. tarasenko, S. Bourelly, and P. Llewellyn, Large and tunable magnetocaloric effect in gadolinium-organic framework: Tuning by solvent exchange, Sci. Rep. **9**, 15572 (2019).
[7] G. Lorusso, J. W. Sharples, E. Palacios, O. Roubeau, E. K. Brechin, R. Sessoli, A. Rossin, F. Tuna, E. J. L. McInnes, D. Collison *et al.*, A dense metal-organic framework for enhanced magnetic refrigeration, Adv. Mater. **25**, 4653 (2013).
[8] J.-J. Yin, T.-Q. Lu, C. Chen, G.-L. Zhuang, J. Zheng, X.-Y. Zheng, and F. Shao, Magnetocaloric effect and slow magnetic relaxation on two-dimensional layered $3d-4f$ cluster-based metal-organic frameworks, Cryst. Growth Des. **20**, 4005 (2020).
[9] P. W. Doheny, S. J. Cassidy, and P. J. Saines, Investigations of the magnetocaloric and thermal expansion properties of the $Ln_3(adipate)_{4.5}(DMF)_2$ (Ln = Gd−Er) framework series, Inorg. Chem. **61**, 4957 (2022).
[10] S. Haldar and S. Ramasesha, Magnetocaloric effect in molecular spin clusters and their assemblies: Exact and Monte Carlo studies using exact cluster eigenstates, J. Magn. Magn. Mater. **500**, 166424 (2020).
[11] M. Gajewski, R. Pelka, M. Fitta, Y. Miyazaki, Y. Nakazawa, M. Balanda, M. Reczynski, B. Nowicka, and B. Sieklucka, Magnetocaloric effect of high-spin cluster with Ni_9W_6 core, J. Magn. Magn. Mater. **414**, 25 (2016).
[12] F. Torres, J. M. Hernández, X. Bohigas, and J. Tejada, Giant and time-dependent magnetocaloric effect in high-spin molecular magnets, Appl. Phys. Lett. **77**, 3248 (2000).
[13] P. Konieczny, D. Czernia, and T. Kajiwara, Rotating magnetocaloric effect in highly anisotropic Tb^{III} and Dy^{III} single molecular magnets, Sci. Rep. **12**, 16601 (2022).
[14] Q.-F. Xu, B.-L. Liu, M.-Y. Ye, L.-S. Long, and L.-S. Zheng, Magnetocaloric effect and thermal conductivity of a 3D coordination polymer of $[Gd(HCOO)(C_2O_4)]_n$, Inorg. Chem. **60**, 9259 (2021).
[15] M. Fitta, W. Sas, and T. Korzeniak, Tunable critical temperature and magnetocaloric effect in ternary Prussian blue analogue, J. Magn. Magn. Mater. **465**, 640 (2018).

[16] M. Fitta, M. Szuwarzyński, P. Czaja, G. Lewińska, and M. Bałanda, The magnetocaloric effect in the thin film of a Prussian blue analogue, Eur. J. Inorg. Chem. **2017**, 4817 (2017).

[17] N. Ma, R. Ohtani, H. M. Le, S. S. Sørensen, R. Ishikawa, S. Kawata, S. Bureekaew, S. Kosasang, Y. Kawazoe, K. Ohara *et al.*, Exploration of glassy state in Prussian blue analogues, Nat. Commun. **13**, 4023 (2022).

[18] Y. Huang and S. Ren, Multifunctional Prussian blue analogue magnets: Emerging opportunities, Appl. Mater. Today **22**, 100886 (2021).

[19] P. Bhatt, M. K. Sharma, M. D. Mukadam, S. S. Meena, and S. M. Yusuf, Electrochemical capacitance and cubic-rhombohedral phase transition of sodium intercalated ferrimagnetic manganese hexacyanoferrate based open framework material, Sustainable Mater. Technol. **35**, e00532 (2023).

[20] A. Kumar, S. M. Yusuf, L. Keller, and J. V. Yakhmi, Microscopic Understanding of Negative Magnetization in Cu, Mn, and Fe Based Prussian Blue Analogues, Phys. Rev. Lett. **101**, 207206 (2008).

[21] P. Bhatt, A. Kumar, S. S. Meena, M. D. Mukadam, and S. M. Yusuf, Magnetic proximity effect in ferrimagnetic-ferromagnetic core-shell Prussian blue analogues molecular magnet, Chem. Phys. Lett. **651**, 155 (2016).

[22] E. Manuel, M. Evangelisti, M. Affronte, M. Okubo, C. Train, and M. Verdaguer, Magnetocaloric effect in hexacyanochromate Prussian blue analogs, Phys. Rev. B **73**, 172406 (2006).

[23] P. Bhatt, S. Banerjee, M. Mukadam, P. Jha, M. Navaneethan, and S. M. Yusuf, Enhanced hydrogen adsorption in alkali metal based copper hexacyanoferrate Prussian blue analogue nanocubes, J. Power Sources **542**, 231816 (2022).

[24] S. Liu, G. L. Pan, G. R. Li, and X. P. Gao, Copper hexacyanoferrate nanoparticles as cathode material for aqueous Al-ion batteries, J. Mater. Chem. A **3**, 959 (2015).

[25] C. D. Wessells, R. A. Huggins, and Y. Cui, Copper hexacyanoferrate battery electrodes with long cycle life and high power, Nat. Commun. **2**, 550 (2011).

[26] H. M. Rietveld, A profile refinement method for nuclear and magnetic structures, J. Appl. Cryst. **2**, 65 (1969).

[27] S. M. Yusuf and L. M. Rao, Magnetic studies in mesoscopic length scale using polarized neutron spectrometer at Dhruva reactor, Trombay, Pramana J. Phys. **47**, 171 (1996).

[28] P. Bhatt, N. Thakur, M. D. Mukadam, S. S. Meena, and S. M. Yusuf, Evidence for the existence of oxygen clustering and understanding of structural disorder in Prussian blue analogues molecular magnet $M_{1.5}[Cr(CN)_6] \cdot zH_2O$ (M = Fe and Co): Reverse Monte Carlo simulation and neutron diffraction study, J. Phys. Chem. C **117**, 2676 (2013).

[29] P. Gütlich, C. Schröder, and V. Schünemann, Mössbauer spectroscopy—An indispensable tool in solid state research, Spectrosc. Eur. **24**, 21 (2012).

[30] P. Gütlich and C. Schröder, Mössbauer spectroscopy, Bunsen-Magazin **12**, 4 (2010).

[31] H. Tokoro, S.-i. Ohkoshi, T. Matsuda, and K. Hashimoto, A large thermal hysteresis loop produced by a charge-transfer phase transition in a rubidium manganese hexacyanoferrate, Inorg. Chem. **43**, 5231 (2004).

[32] K. Wataru, I. Tohru, Y. Hisashi, T. Yayoi, H. Kazuhito, and O. Shin-ichi, Synthesis of ferromagnetic CsCuCr Prussian blue analogue with a tetragonal structure, Chem. Lett. **34**, 1278 (2005).

[33] M. D. Mukadam, A. Kumar, S. M. Yusuf, J. V. Yakhmi, R. Tewari, and G. K. Dey, Spin-glass behavior in ferromagnetic $Fe[Fe(CN)_6] \cdot xH_2O$ nanoparticles, J. Appl. Phys. **103**, 123902 (2008).

[34] M. D. Mukadam, S. M. Yusuf, P. Sharma, S. K. Kulshreshtha, and G. K. Dey, Dynamics of spin clusters in amorphous Fe_2O_3, Phys. Rev. B **72**, 174408 (2005).

[35] V. K. Anand, L. Opherden, J. Xu, D. T. Adroja, A. D. Hillier, P. K. Biswas, T. Herrmannsdörfer, M. Uhlarz, J. Hornung, J. Wosnitza *et al.*, Evidence for a dynamical ground state in the frustrated pyrohafnate Tb_2Hf_2O, Phys. Rev. B **97**, 094402 (2018).

[36] N. Hanasaki, K. Watanabe, T. Ohtsuka, I. Kézsmárki, S. Iguchi, S. Miyasaka, and Y. Tokura, Nature of the Transition between a Ferromagnetic Metal and a Spin-Glass Insulator in Pyrochlore Molybdates, Phys. Rev. Lett. **99**, 086401 (2007).

[37] L. J. V. Stimpson, J. M. Powell, G. B. G. Stenning, M. Jura, and D. C. Arnold, Spin-glass behavior in $K_xRu_{4-y}Ni_yO_8$ hollandite materials, Phys. Rev. B **98**, 174429 (2018).

[38] A. Kumar, A. Senyshyn, and D. Pandey, Evidence for cluster spin glass phase with precursor short-range antiferromagnetic correlations in the B-site disordered $Ca(Fe_{1/2}Nb_{1/2})O_3$ perovskite, Phys. Rev. B **99**, 214425 (2019).

[39] W. E. Buschmann, J. Ensling, P. Gütlich, and J. S. Miller, Electron transfer, linkage isomerization, bulk magnetic order, and spin-glass behavior in the iron hexacyanomanganate Prussian blue analogue, Chem. Eur. J **5**, 3019 (1999).

[40] W. E. Buschmann and J. S. Miller, Magnetic ordering and spin-glass behavior in first-row transition metal hexacyanomanganate(IV) Prussian blue analogues, Inorg. Chem. **39**, 2411 (2000).

[41] B. Gao, J. Yao, and D. Xue, Vacancy-induced spin-glass behavior of Prussian blue analogue $Fe^{II}_{1.1}Cr^{II}_x[Cr^{III}(CN)_6]_{0.6-x} \cdot nH_2O$ nanowires, J. Magn. Magn. Mater. **322**, 2505 (2010).

[42] L. Lartigue, S. Oh, E. Prouzet, Y. Guari, and J. Larionova, Superspin-glass behavior of $Co_3[Fe(CN)_6]_2$ Prussian blue nanoparticles confined in mesoporous silica, Mater. Chem. Phys. **132**, 438 (2012).

[43] B. Gao, J. Yao, and D. Xue, Spin-glass behavior of the polyvinyl pyrrolidone-protected Prussian blue analog $K_{1.14}Mn[Fe(CN)_6]_{0.88}$ nanocubes, Phys. B: Condens. Matter **406**, 2528 (2011).

[44] M. Ghanathe, A. Kumar, and S. M. Yusuf, Microscopic and mesoscopic understanding of magnetization compensation phenomenon in ferrimagnetic $Li_{0.5}FeCr_{1.5}O_4$ spinel, J. Appl. Phys. **125**, 093903 (2019).

[45] I. Dhiman, A. Das, R. Mittal, Y. Su, A. Kumar, and A. Radulescu, Diffuse neutron scattering study of magnetic correlations in half-doped $La_{0.5}Ca_{0.5-x}Sr_xMnO_3$ manganites (x = 0.1, 0.3, and 0.4), Phys. Rev. B **81**, 104423 (2010).

[46] S. M. Yusuf and A. Kumar, Neutron scattering of advanced magnetic materials, Appl. Phys. Rev. **4**, 031303 (2017).

[47] M. Evangelistia, E. Manuel, M. Affrontea, M. Okubo, C. Trainc, and M. Verdaguer, Vacancy-driven magnetocaloric effect in Prussian blue analogues, J. Magn. Magn. Mater. **316**, e569 (2007).

[48] H. Oesterreicher and F. T. Parke, Magnetic cooling near Curie temperatures above 300 K, J. Appl. Phys. **55**, 4334 (1984).